Emission Polarization of Europium and Terbium Chelates

Jeff G. Reifenberger, Gregory E. Snyder, Gordon Baym, and Paul R. Selvin*

Physics Department, University of Illinois, Urbana, Illinois 61801

Received: June 19, 2003; In Final Form: September 23, 2003

We measured the anisotropy of Tb^{3+} and Eu^{3+} in various chelate complexes bound with or without a carbostyril antenna. The anisotropy of the lanthanides depends on the chelate as well as whether the antenna is present. The anisotropy of Eu^{3+} bound to only a chelate is high while for Tb^{3+} the anisotropy is nearly zero. For Eu^{3+}, the anisotropy decreases upon addition of the antenna, while for Tb^{3+} the anisotropy slightly increases once the antenna is attached. A theoretical model is discussed to account for the measured anisotropy of the Eu^{3+} bound to the chelate and how the addition of the antenna affects the anisotropy. While the transitions within Tb^{3+} are more complicated than those in Eu^{3+}, the theoretical model is also extended to Tb^{3+} to explain qualitatively how the addition of the antenna affects the measured anisotropy of the terbium complex. Because of their low anisotropy, both Tb^{3+} and Eu^{3+}, when bound to a chelate with an antenna, are ideal luminescent probes in resonance energy transfer experiments for measuring nanometer scale distances. Our results indicate that it may be possible to construct a probe with Eu^{3+} that retains its high anisotropy once the antenna is added to the chelate complex. This probe could measure rotational motion on the millisecond lifetime.

I. Introduction

Luminescent lanthanide chelate complexes, particularly those containing Tb^{3+} and Eu^{3+}, are of great interest as alternatives to conventional organic-based fluorescent probes. Figure 1 shows a representative complex; it contains a chelate, diethylenetriaminepentacetic acid (DTPA) or triethylenetetraaminehexaacetic acid (TTHA), that shields the lanthanide from quenching by water and an organic-based antenna molecule, carbostyril 124 (cs124), that efficiently absorbs excitation light and transfers excitation energy to the lanthanide. In such a complex, Tb^{3+} and Eu^{3+} have unusual spectroscopic characteristics even in an aqueous environment when compared to organic fluorophores. These include millisecond lifetimes, sharply spiked emission spectra, high quantum yield, and a broad range of emission energies extending from the blue to the red parts of the spectrum.[1] Another important property is their emission polarization, which is the subject of this paper. Low polarization is desired when using lanthanide chelates in resonance energy transfer experiments to measure nanometer-scale conformational changes of biomolecules.[1] High polarization is desired if using the chelates as probes to measure rotational motion on the millisecond time scale.[2]

The emission spectrum of lanthanide chelates arises from high-spin−high-spin transitions within the atom. Tb^{3+} emission arises from transitions between a $^5D_4$ excited state to a ground state of ^7F_J ($J = 0-6$). Eu^{3+} emission is from a $^5D_0$ to a ground state of ^7F_J ($J = 0-6$) (see Figure 2). In both cases, the ground and excited states involve 4f electrons, and hence, electric dipole transitions, the usual mechanism of fluorescence in organic dyes, are formally parity forbidden. Nevertheless, a small admixture of 5d states makes electric dipole transitions possible. Much
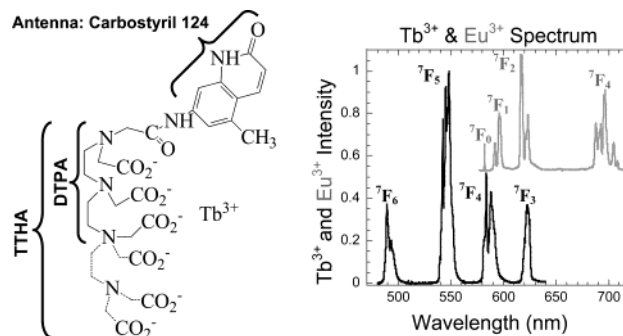
* To whom correspondence should be addressed. Loomis Laboratory of Physics, 1110 W. Green St., Urbana, IL 61801. E-mail: selvin@uiuc.edu. Tel: (217) 244−3371. Fax: (217) 244-7559.

Figure 1. Structure and spectra of lanthanide chelate with antenna. The chemical structure of Tb−DTPA(TTHA)−cs124 along with characteristic spectrum of both Tb^{3+} (black) and Eu^{3+} (gray). Without the carbostyril antenna, the lanthanide directly absorbs the incident photon at 488 nm for Tb^{3+} or 576 nm for Eu^{3+}. With the antenna, absorption occurs at 337 nm by the antenna and the energy is then transferred to the lanthanide.

work has been done to understand the intensities, wavelengths, and origin of the lanthanide emission transitions in a crystal field.[3−6] Indeed, emission generally arises from electric dipole transitions, although magnetic dipole transitions exist, e.g., the $^5D_0$ to $^7F_1$ transition in europium,[7,8] and in the solid state, electric quadrupole transitions have been detected.[9]

Most of the Tb^{3+} and Eu^{3+} transitions have multiple transition dipole moments because emission can arise from multiple m_J levels. Hence, if these transitions are energetically degenerate (or nearly so), and the probability of emission due to each state is similar, then the emission will be unpolarized. Lanthanide emission has generally been assumed to be unpolarized due to these factors. Rotational motion during the millisecond lifetime of the lanthanide bound to the chelate−carbostyril complex can also lead to depolarization, particularly in solution.

Transitions between europium's excited $^5D_0$ state, unlike terbium's excited $^5D_4$ state, are not degenerate and therefore

Emission Polarization of Europium and Terbium Chelates

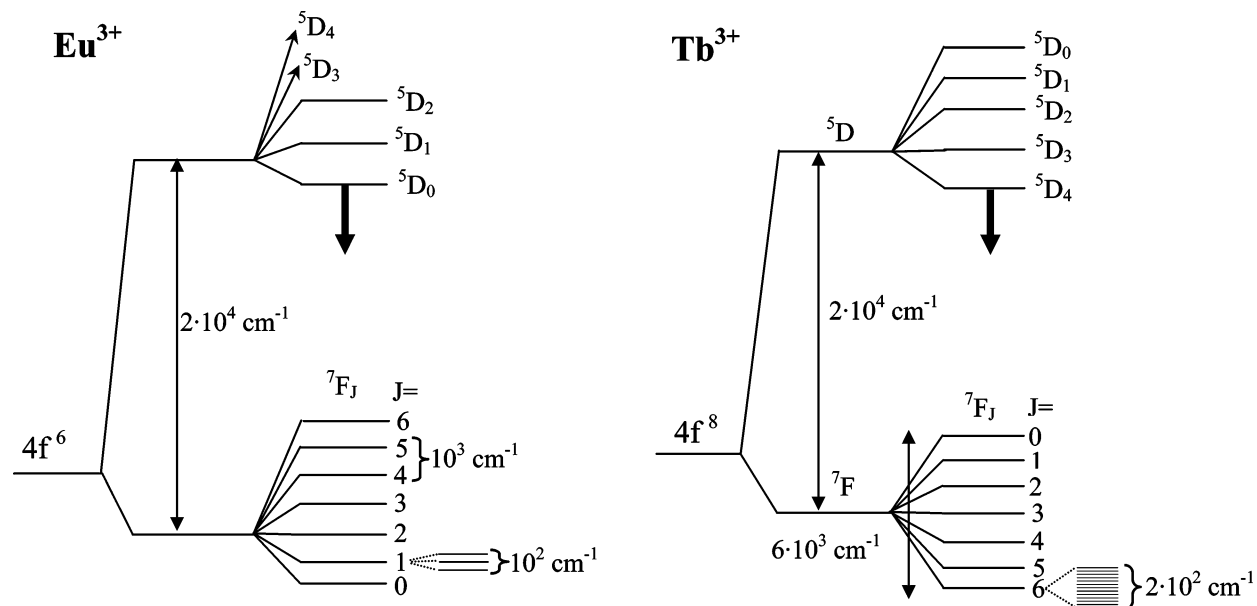*J. Phys. Chem. B, Vol. 107, No. 46, 2003* **12863**

Figure 2. Energy levels of lanthanides. We studied the $^5D_0 \rightarrow {}^7F_J$ ($J = 0-4$) transition for Eu^{3+} and the $^5D_4 \rightarrow {}^7F_J$ ($J = 4-6$) transition for Tb^{3+}. The splittings are, from left to right, due to interelectronic repulsion, spin−orbit coupling, and ligand-field effects (the splitting of the individual J states). Figure from ref 8.

can lead to spectra that have a high anisotropy (e.g., $^5D_0 \rightarrow {}^7F_0$). Previous work has shown that Eu^{3+} emission can indeed be polarized if excited directly (i.e., not through an antenna) when in a single crystal of $Zn_3Eu_2(NO_3)_{12} \cdot 24H_2O$.[10] Vereb et al. have also shown that emission of Eu−DTPA−cs124 in a crystal is polarized.[11] They showed that all the transitions within the europium were polarized to some degree with the $^5D_0 \rightarrow {}^7F_0$ transition ($m_J = 0$ for excited and ground states) being the most polarized. However it is unclear if the nonzero anisotropy was due to crystal conditions, e.g., the crystal imposed a fixed orientation between the antenna and the lanthanide and chelate. Also, no measurements were made on the anisotropy of Eu−DTPA or Tb−DTPA after direct excitation but instead only excitation through the antenna. For measurements in this paper, the lanthanide chelates both with and without the antenna are not in a crystal but rather frozen in an amorphous glass. This provides for a random distribution of lanthanide chelates.

We examine the emission polarization of two polyamino-carboxylate chelates, DTPA and TTHA, with and without an antenna molecule, carbostyril 124, bound to either Eu^{3+} or Tb^{3+} frozen in an amorphous glass. Without the antenna, the lanthanide was excited directly (488 nm for Tb^{3+}, 576 nm for Eu^{3+}). With the antenna, excitation of the lanthanide was indirect at 337 nm, where the antenna absorbs strongly (and direct lanthanide excitation is negligible). Tb^{3+} bound to either chelate (DTPA or TTHA) without an antenna was unpolarized and, surprisingly, became (weakly) polarized when excited through the antenna. Eu^{3+} excited directly was highly polarized, while excitation through the antenna led to a lower polarization. These results indicate that lanthanides are excellent donors in resonance energy transfer applications, especially terbium, when excited through the antenna. The fact that the anisotropy increases upon the addition of the antenna (especially with Tb−TTHA) suggests the possibility of highly polarized lanthanide probes if the antenna and lanthanide can be oriented properly.

II. Experimental Section

Sample Preparation. The lanthanide atoms and the chelates (both DTPA and TTHA) were purchased from Sigma. Synthesis and purification of DTPA−cs124 and TTHA−cs124 has been

described previously.[12] The chelates, both with and without carbostyril 124, are mixed with $TbCl_3$ or $EuCl_3$ such that the ratio of lanthanide salts to chelate (with and without the antenna) is 0.8. This ensures that all of the lanthanides are attached to a chelate, i.e., no free lanthanides are in the solution. The pH is then adjusted to pH 7, and the solution is added to glycerol such that the percentage of water by volume in the entire mixture is 40%. The final concentration of lanthanide chelates in glycerol is 0.13 M for lanthanides attached to DTPA and 0.11 M for the lanthanides attached to TTHA. The final concentration for the lanthanides attached to both DTPA−cs124 and TTHA−cs124 is 1.6 μM. The glycerol/water mixture also contains 1 M NaCl, in addition to the lanthanide chelates (with and without the antenna), to improve the optical quality of the glycerol−water solution when frozen.

The mixture described above is then frozen in a temperature-controlled laboratory-built Dewar cooled by liquid nitrogen, which contains optically clear quartz windows for right angle excitation and luminescence detection. The temperature is monitored by a thermocouple placed in the top of the glycerol solution containing the lanthanide chelates. Glycerol forms an amorphous glass when frozen that immobilizes the lanthanide−chelate−carbosytril complexes. To ensure that the sample was frozen (i.e., not rotating during the measurement), the anisotropy of the $^5D_0 \rightarrow {}^7F_0$ transition within Eu−DTPA was monitored and found to not change for a temperature range of −68 to −90 °C (data not shown). A change in the anisotropy was measured at higher temperatures indicating that the molecule had moved during the measurement. However all anisotropy data presented in this paper was collected in a temperature region of −80 to −90 °C. When the antenna is attached, excitation of either Tb^{3+} or Eu^{3+} occurs indirectly through the antenna by excitation at 337 nm. Without the antenna, direct excitation of the Tb^{3+} is at 488 nm and of the Eu^{3+} is at 578 nm.

Anisotropy Measurements. The anisotropy was measured by standard methods, including right angle excitation and emission collection with polarizers in both pathways. Details of the instrumentation can be found elsewhere.[13] Briefly, the sample is excited by a pulsed nitrogen laser with optional dye housing and the emitted light is collected with an imaging

spectrometer utilizing a 1200 grooves/mm grating and charge-coupled detector (CCD) for acquisition of the emission spectrum of the lanthanides. A mechanical chopper is placed in front of the spectrometer and timed such that the entrance slit to the spectrometer is blocked for ∼20 μs after the laser was fired. This prevents the laser pulse and prompt fluorescence of the sample from reaching the CCD camera. With the chopper, a ∼40000-fold suppression of prompt fluorescence is achieved. After the emitted light is collected from the sample with the CCD camera, the anisotropy at each wavelength is calculated according to standard methods[14]

$$r = \frac{I_{\|} - I_{\perp}}{I_{\|} + 2I_{\perp}} \quad (1)$$

$I_{\|}$ is the intensity of the emitted light when the emission polarizer is oriented parallel to the direction of the excitation polarization, while $I_{\perp}$ is the intensity of emitted light when the emission polarizer is perpendicular to the direction of the polarized excitation. Both intensities ($I_{\|}$ and $I_{\perp}$) have been normalized to correct for the polarization sensitivity of the detection pathway.[14] The resolution of the instrument is tested by measuring the room light's spectrum while using the same slit width, grating, etc. that are used in the actual experiment. The wavelength resolution for Eu−DTPA/Eu−TTHA samples is 2.5 Å, while for all other samples the resolution is 1.2 Å.

III. Theory

The measured anisotropy, the splitting and mixing of the m_J states, and the relative intensity of Tb^{3+} or Eu^{3+} transitions, excited directly or through the carbostyril antenna, can be understood in terms of the quantum mechanical symmetries under rotation of the states excited by the incident laser. We first consider in detail Eu^{3+}. We assume that the excited states can be described within the Russell−Saunders model and neglect small mixing with other states (e.g., vibronic states). We take the rotational symmetry explicitly into account by calculating absorption and emission matrix elements in terms of single particle spherical harmonics, Y_{Jm}, which, from the Wigner−Eckhardt theorem, are proportional to the exact matrix elements. For parameters such as the anisotropy that depend on a ratio of measured parameters, the proportionality constants drop out. The absolute energy levels (emission wavelengths) are a function of the constants, but the relative energy levels (wavelength splittings), which are of greater interest, are independent of the constants. Figure 2 shows the energy levels involved in the transitions within both the Tb^{3+} and Eu^{3+} atoms. The electric field that holds the lanthanide ion in place not only splits and mixes the m_J states within the lanthanide ion but allows transitions, which are formally forbidden in the free ion, to occur.

All the transitions in the lanthanide ion that we study are electric dipole, with the exception of the $^5D_0 \rightarrow {}^7F_1$, transition within Eu^{3+}, which is a magnetic dipole transition.[8] The anisotropy of processes involving magnetic dipole transitions, as we will show, differs from that in purely electric dipole transitions. We first derive the anisotropy for electric dipole transitions and then discuss the case of magnetic dipole transitions. To measure the anisotropy, an external photon polarized in the $\hat{z}$ direction is sent along the x axis and absorbed by an electric dipole moment with matrix element u between the initial and intermediate states (see Figure 3). The photon is subsequently reemitted and polarized in the $\hat{w}$ direction by an electric dipole moment with matrix element v between the
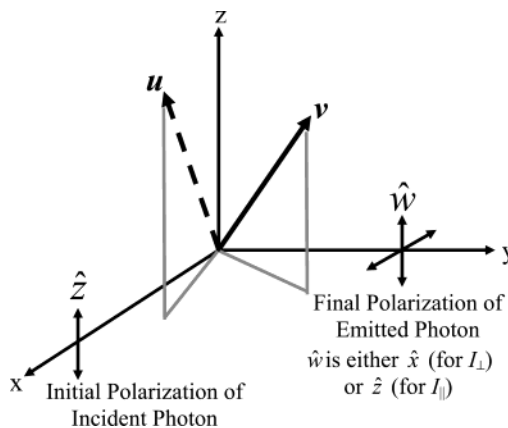

Figure 3. Experimental setup. A laser sends a photon along the x axis, polarized in the z direction, to excite the lanthanide's or the antenna's absorption dipole moment, u. After it is returned to its ground state, the lanthanide emits a photon from its emission dipole moment, v, which is not necessarily parallel to u. A polarizer is used to select either a polarization of z or x before the emitted light is detected by a CCD camera.

intermediate and final states. The intensity of this transition is, to within an overall constant

$$I_w = \int \frac{d\Omega}{4\pi} |\hat{z} \cdot u|^2 |\hat{w} \cdot v|^2 \quad (2)$$

Here Ω is the solid angle specifying all the orientations of the chelate. The integration is an average over all orientations of the chelate since the sample is randomly oriented when frozen.

The first term in eq 2, $\hat{z} \cdot u$, is proportional to the probability that the lanthanide is excited by the incident photon, while the second term, $\hat{w} \cdot v$, is proportional to the probability that a photon is emitted from the lanthanide atom polarized in the $\hat{w}$ direction. For $I_{\|}$ (eq 1), $\hat{w}$ is in the z direction, while for $I_{\perp}$, $\hat{w}$ is in the x direction (see Figure 3). While for most organic fluorophores u and v are parallel (or nearly parallel) to each other, it is certainly not required. In fact, u and v tend to not be parallel for lanthanide atoms in a crystal field. For arbitrary orientations of the absorption and emission dipole moments, the angular average in eq 2 simply gives

$$I = \frac{1}{15}(2 - \cos^2\theta) + \frac{1}{30}(3\cos^2\theta - 1)(|\hat{u} \cdot \hat{v}|^2 + |\hat{u} \cdot \hat{v}^*|^2) \quad (3)$$

where $\hat{u}$ and $\hat{v}$ denote the (possibly complex) unit vectors in the direction of the dipole moment matrix elements. The angle θ is the angle between the initial polarization of the incident photon and the polarization of the emitted photon (for $I_{\|}$, $\theta = 0°$; for $I_{\perp}$, $\theta = 90°$). As we shall see, $\hat{u}$ points along a specific direction in the lanthanide frame and thus is real to within an overall phase factor, which drops out. In this case, $|\hat{u} \cdot \hat{v}|^2 = |\hat{u} \cdot \hat{v}^*|^2$ and eq 3 reduce to

$$I_{\|} = \frac{1}{15}(1 + 2(\hat{u} \cdot \hat{v})^2) \qquad I_{\perp} = \frac{1}{15}(2 - (\hat{u} \cdot \hat{v})^2) \quad (4)$$

The expression for the anisotropy in eq 1 is simplified to

$$r_{el-el} = \frac{1}{5}(3(\hat{u} \cdot \hat{v})^2 - 1) \quad (5)$$

Generally, $-0.2 \leq r \leq 0.4$; if u and v are parallel, $r = 0.4$, while if they are perpendicular, $r = -0.2$.

Emission Polarization of Europium and Terbium Chelates

J. Phys. Chem. B, Vol. 107, No. 46, 2003 **12865**

Equation 5 is the standard expression for anisotropy when the absorption and emission of a photon are through an electric dipole transition.[2] As mentioned above, the absorption of a photon in Eu^{3+} is through an electric dipole but the transition, $^5D_0 \rightarrow {}^7F_1$, is a magnetic dipole. In such a transition, the coupling of the photon is via the operator $-\vec{H}\cdot\vec{M}$, where $\vec{M}$ is the magnetic moment operator of the atom and $\vec{H}$ is the magnetic field of the photon. The magnetic field of the photon can be written in terms of an electric field, $\vec{E}$, and the direction of motion of the photon, $\hat{n}$, by the following expression: $\vec{H} = \vec{E} \times \hat{n}$. Consider first a magnetic dipole absorption transition followed by a magnetic dipole emission transition for the geometry in Figure 3. In this case, the magnetic field of the incident photon is in the y direction and that of the emitted photon is in the $\hat{w} \times \hat{y}$ direction, where w is the measured direction of the electric field of the final photon. The intensity is then, to within a constant

$$I_w = \int \frac{d\Omega}{4\pi} |\hat{y}\cdot\vec{u}_m|^2 |\hat{w} \times \hat{y}\cdot\vec{v}_m|^2 \tag{6}$$

where $\vec{u}_m$ is the magnetic dipole absorption matrix element and $\vec{v}_m$ the magnetic dipole emission matrix element. Then

$$I_\parallel^{mag-mag} = I_\perp^{mag-mag} = \frac{1}{30}(4 - |\hat{u}_m\cdot\hat{v}_m|^2 - |\hat{u}_m\cdot\hat{v}_m^*|^2) \tag{7}$$

and the anisotropy vanishes.

On the other hand, consider an electric dipole absorption followed by a magnetic dipole photon emission, e.g., $^7F_0 \rightarrow {}^5D_0$ followed by $^5D_0 \rightarrow {}^7F_1$. If an electric dipole moment parallel to the z axis emits a photon in the y direction, the photon will be polarized along the z direction; while if a magnetic dipole parallel to the z direction emits a photon traveling along the y direction, the electric field will be along the x direction. The intensity is, to within a constant

$$I_\parallel^{el-mag} = \frac{1}{15}(2 - (\hat{u}\cdot\hat{v}_m)^2) \qquad I_\perp^{el-mag} = \frac{1}{15}(1 + 2(\hat{u}\cdot\hat{v}_m)^2) \tag{8}$$

where for simplicity we have taken v_m to be real. We immediately see that, unlike the previous case (absorption and emission through a magnetic dipole), the anisotropy does not vanish for an absorption through an electric dipole followed by an emission through a magnetic dipole. The expressions for the parallel and perpendicular intensities are interchanged from that of the electric dipole–electric dipole case. In this case, the anisotropy is given by

$$r_{el-mag} = \frac{1 - 3(\hat{u}\cdot\hat{v}_m)^2}{4 + 3(\hat{u}\cdot\hat{v}_m)^2} \tag{9}$$

Then $-2/7 \leq r \leq 1/4$; when the absorption dipole moment is parallel to the emission dipole moment $r = -2/7$, while if they are perpendicular, $r = 1/4$. This range of anisotropies is quite different than that for electric dipole emission.

Let us now consider the algebraic structure of the matrix elements entering the intensities. The electrons in the f shell of the lanthanide atom all have the same radial wave function, and for understanding the relative strength of transitions involving only the f shell, the properties of the radial wave function are not relevant. The algebraic properties of the various states $|^7F_{J,m}\rangle$ shown in Figure 2 are the same as a single electron in an angular state, $Y_{Jm}(\theta,\phi)$. The matrix element for

the transition $^7F_0 \rightarrow {}^5D_0$ in Eu^{3+} is given by

$$\vec{u} = \langle{}^5D_0|\vec{d}|^7F_0\rangle \tag{10}$$

The electric transitions $^7F_J \rightarrow {}^5D_0$, are forbidden by parity conservation in the free atom, where the states $|^7F_{J,m}\rangle$ as well as $|^5D_0\rangle$ have even parity. In order for the electric dipole matrix elements between these states to be nonvanishing, the states must have a small admixture of odd parity states caused by the "crystal field" felt by the lanthanide in the chelate. We define the z axis in the local frame of the lanthanide (not to be confused with the z axis in the lab frame depicted in Figure 3) by the direction of the electric dipole matrix element $\langle{}^5D_0|\vec{d}|^7F_0\rangle$, where $\vec{d}$ is the electric dipole operator. (From here on, the unprimed (x,y,z) coordinate system refers to the lanthanide frame, i.e., defined such that u is along the z direction. The anisotropy is only a function of the angle between u and v. Then the emission electric dipole matrix elements, $\langle{}^7F_{J,m}|\vec{d}|^5D_0\rangle$, have the same algebraic structure as $\int d\Omega Y_{Jm}^*(\theta,\phi)\vec{r}\cos\theta$. Similar expressions can be written for $\vec{u}$ and $\vec{v}$ for Tb^{3+}. However, an exact direction of $\vec{u}$ and $\vec{v}$ for Tb^{3+} cannot be easily determined due to the complexity of the wave functions of ground state ^7F_J and the excited state $^5D_4$.

Magnetic dipole interaction among f shell electrons are allowed by parity, and thus an admixture is not required for a transition; thus the magnetic dipole matrix element

$$\vec{v}_m = \langle{}^7F_{1,m}|\vec{M}|^5D_0\rangle \tag{11}$$

for the process $^5D_0 \rightarrow {}^7F_{1,m}$ has the same algebraic structure as $\int d\Omega Y_{1m}^*(\theta,\phi)\vec{r}$.

IV. Results and Discussion

Eu–DTPA. Of the four transitions within the Eu^{3+} that we study, the first, $^5D_0 \rightarrow {}^7F_0$, is the easiest to understand. As mentioned above, $\vec{u}$ is defined to be along the z direction. The direction of $\vec{v}$ has the form

$$\vec{v} \propto \int \frac{d\Omega}{4\pi} \vec{r}z = \hat{z} \tag{12}$$

Since $\vec{v}$ is parallel to $\vec{u}$, eq 5 predicts that the anisotropy of this transition is 0.4 and is almost what is seen in the $^7F_0$ panel in Figure 4. The measured value for the anisotropy, 0.37 ± 0.01, is a little less than the theoretical value of 0.4. This ~8% discrepancy is probably due to the fact that although the samples were frozen in an amorphous glass, they are able to undergo small rotation during the ~1 ms long lifetime of the $^5D_0$ intermediate state, decreasing the anisotropy of the sample. Because of the resolution of the spectrometer and the fact that there is no degeneracy in the $^5D_0 \rightarrow {}^7F_0$ transition within Eu–DTPA, the full width at half maximum (fwhm) of the transition should have been close to 2.5 Å. However the fwhm was measured to be ~5 Å. This may be due to the fact that Eu–DTPA has several different conformations. The different conformations would each lead to a different physical environment for Eu^{3+} and hence create an overall broadening of the $^5D_0 \rightarrow {}^7F_0$ line. The $^5D_0 \rightarrow {}^7F_0$ transition is the simplest case although it is representative of the physics in the other three more complicated transitions.

Figure 4 shows three lines in the $^5D_0 \rightarrow {}^7F_1$ transition. In the free atom, these lines are degenerate. The present splitting is due to the crystal field, $V(\vec{r})$, felt by the electrons within the lanthanide from the chelate. Before analyzing these lines, we need to discuss the crystal field. The potential energy due to
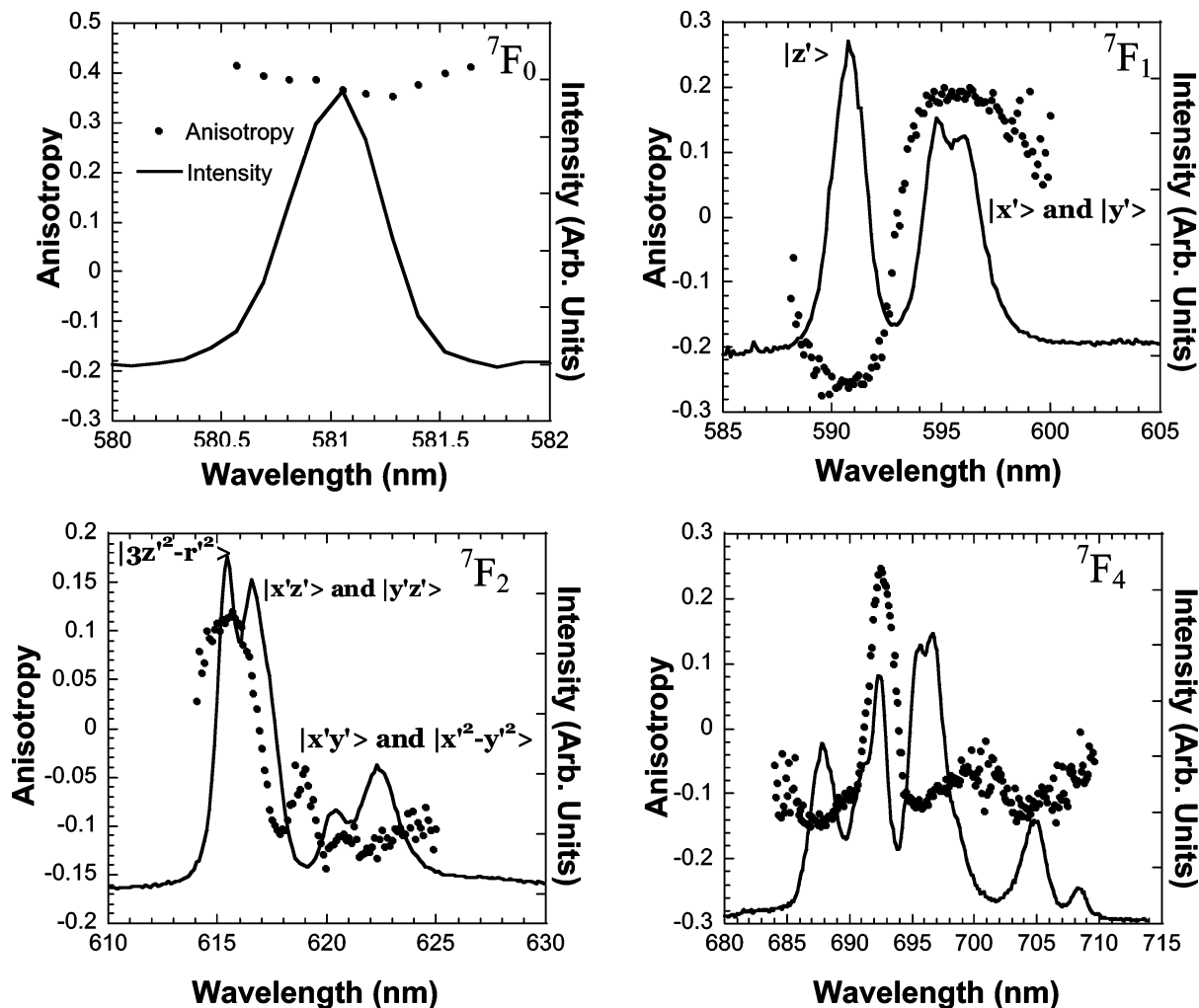
Figure 4. Anisotropy of Eu−DTPA. The black dots are the anisotropy. The measured intensity (arbitrary units) of each transition is shown with a black line. Each state, ^7F_J, is labeled in the upper right corner of every plot while the wave function is next to the actual spectral line of the transition to the $^7F_1$ and $^7F_2$ states.

the surrounding charge density, ρ, has the form: $V(\vec{r}) = e \int d^3r' \rho(r')/|\vec{r} - \vec{r}'|$. For the orbits of interest, $r < r'$, and we can expand the potential in terms of spherical harmonics in the form

$$V(\vec{r}) = \sum_l V_l(\vec{r}) = \sum_{l,m} c_{lm} r^{l+1} Y_{lm}(\theta, \phi) \qquad (13)$$

The term V_0 gives rise to a shift of the atomic levels, which is the same for states involving electrons in the f shell. It thus drops out of the measured $^5D_0 \rightarrow {}^7F_J$ transition frequencies, and we ignore it in the following. The odd l terms (V_1, V_3, etc.) are responsible for the parity admixture that allows transitions between states of the same parity in the free atom. The even l terms (V_2, V_4, etc.) are responsible for the splitting and mixing of the J,m states.[3] The term V_1 has the structure

$$V_1 = c_{1,m} r^2 \hat{a} \cdot \hat{r} \qquad (14)$$

where the direction $\hat{a}$ is a property of the lanthanide. As discussed above, the electric dipole moment is along the direction $\hat{a}$, which we define to be the z axis in the local frame of the lanthanide; thus $V_1 \sim z$.

In the subspace of the $^7F_1$ states, only the matrix elements of V_2 are nonvanishing, by the rules of addition of angular momentum. The component V_2 has the angular structure $\sum_{ab} \epsilon_{ab} r_a r_b / r^2$, where the ϵ_{ab} values are real. One can always choose a (primed) coordinate system that diagonalizes this

to a quadratic form, so that the angular structure of V_2 becomes

$$V_2 \sim (\alpha x'^2 + \beta y'^2 + \gamma z'^2)/r^2 \qquad (15)$$

where $\alpha + \beta + \gamma = 0$. The eigenstates in the $^7F_1$ subspace, found by applying degenerate perturbation theory, are the Cartesian states $|z'\rangle$ with wave function $\sim Y_{1,0}$, $|x'\rangle$ with wave function $\sim Y_{1,1} + Y_{1,-1}$, and $|y'\rangle$, with wave function $\sim Y_{1,1} - Y_{1,-1}$. The radial integrals give an overall constant which we absorb in the definition of α, β, and γ. The corresponding energy shifts due to V_2 are then

$$\Delta E_x = \frac{3}{5}\alpha + \frac{1}{5}(\beta + \gamma) = \frac{2}{5}\alpha \quad \Delta E_y = \frac{2}{5}\beta \quad \Delta E_z = \frac{2}{5}\gamma$$
$$(16)$$

where the factor $^3/_5$ is the angular average, $\int(d\Omega/4\pi) \cos^4 \theta / \int(d\Omega/4\pi) \cos^2 \theta$, and the $^1/_5$ is the angular average, $\int d\Omega/4\pi \cos^2 \theta \sin^2 \theta \cos^2 \phi / \int d\Omega/4\pi \cos^2 \theta$. Fitting to the shifts of the wavelengths of the three $^5D_0 \rightarrow {}^7F_1$ transitions, we find $\alpha \cong -(^{25}/_3)$ meV, $\beta \cong -(^{55}/_3)$ meV, and $\gamma \cong (^{80}/_3)$ meV.

Note that the primed coordinate system in the lanthanide's frame need not be aligned along the z direction (which was defined to be the direction of u, the absorption dipole moment). In other words, there can be a slight rotation, although as we discuss below, this rotation is small. If we assume that the z' and z axes coincide, then for the state $|z'\rangle$, v_m is also in the z

Emission Polarization of Europium and Terbium Chelates

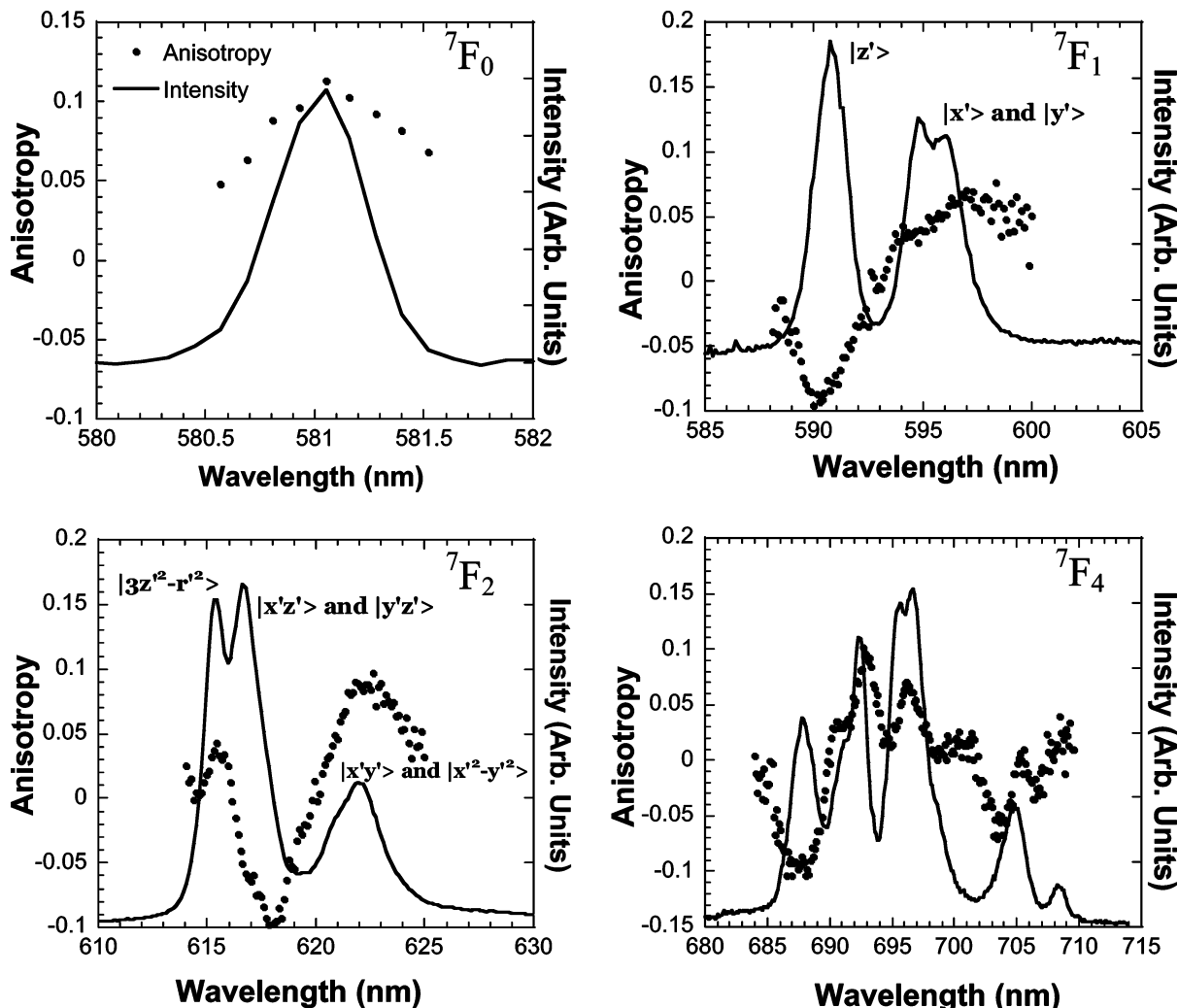*J. Phys. Chem. B, Vol. 107, No. 46, 2003* **12867**

Figure 5. Anisotropy of Eu−DTPA−cs124. The anisotropy data are shown as the black dots. The measured intensity (arbitrary units) of each transition is shown with a black line. Each state, ^7F_J, is labeled in the upper right corner of every plot while the wave function is next to the actual spectral line of the transition to the $^7F_1$ and $^7F_2$ states.

direction, with a corresponding anisotropy $-2/7$, according to eq 9. In the states $|x'\rangle$ and $|y'\rangle$, v_m is perpendicular to $\hat{z}$, and thus from eq 9 we would infer that both these states have anisotropy $1/4$.

Figure 4 shows that the observed anisotropies, -0.25 and 0.19, for the three lines are close but not quite equal to the calculated values. The differences from the observed and calculated values is due to the fact that the emission dipole moment, v_m, is not quite aligned with (or orthogonal to) the absorpton dipole moment, u, i.e., the primed frame is not quite aligned along the z axis. One can transform between the absorption dipole moment frame and the emission dipole moment frame by writing

$$\hat{z} = A\hat{x}' + B\hat{y}' + C\hat{z}' \qquad (17)$$

where $A^2 + B^2 + C^2 = 1$.

By use of the above transformation, $(\hat{u}\cdot\hat{v}_m)^2 = C^2$ in the state $|z'\rangle$. Associating this state with the highest energy line, with anisotropy $\cong -0.25$, implies that $C^2 \cong 0.92$. Since the anisotropy of $|x'\rangle$ and $|y'\rangle$ are approximately the same, we can assume that $A^2 \cong B^2 \cong 0.04$, which leads to an anisotropy of these states, $\cong 0.21$, quite close to the measured value $\cong 0.19$. We find the closest fit to both the $^7F_1$ and $^7F_2$ eigenstates with the values $C^2 \cong 0.84$ and $A^2 \cong B^2 \cong 0.08$, which imply anisotropies of the three $^7F_1$ eigenstates of -0.23 and 0.18. The

TABLE 1: Theoretical and Experimental Values of the Anisotropy of Eu−DTPA[a]

wave functions	wavelength[b] (nm)	calculated anisotropy	measured anisotropy	calculated relative intensity
		$^7F_1$ State		
$|x'\rangle$	594.8	0.18	0.19	0.33
$|y'\rangle$	596.0	0.18	0.19	0.33
$|z'\rangle$	590.8	-0.23	-0.25	0.33
		$^7F_2$ State		
$|3z'^2 - r'^2\rangle$	(615.4) 615.4	0.19	0.12	0.62
$|z'y'\rangle$	(616.2) 618.0	-0.03	0.00	0.16
$|z'x'\rangle$	(617.0) 618.9	-0.03	0.00	0.16
$|x'y'\rangle$	(619.9) 622.1	-0.10	-0.14	0.03
$|x'^2 - y'^2\rangle$	(620.0) 620.4	-0.20	-0.12	0.03

[a] Columns 3 and 4 compare calculated values vs measured values of Eu−DTPA anisotropy. The relative intensities were determined from the emission dipole moment squared: $|\bar{v}|^2$. [b] The $^7F_1$ wavelengths listed are the measured values and are used to fit α, β, and γ of the V_2 potential. The values α, β, and γ are then used to calculate the splittings of the $^7F_2$ state.

relative intensities of the three transitions are proportional to $|v_m|^2$, which is the same for all three lines, in reasonable agreement with the data.

The transitions to the $^7F_2$ states are more complicated since their anisotropies and splittings depend on both V_2 and V_4 (but
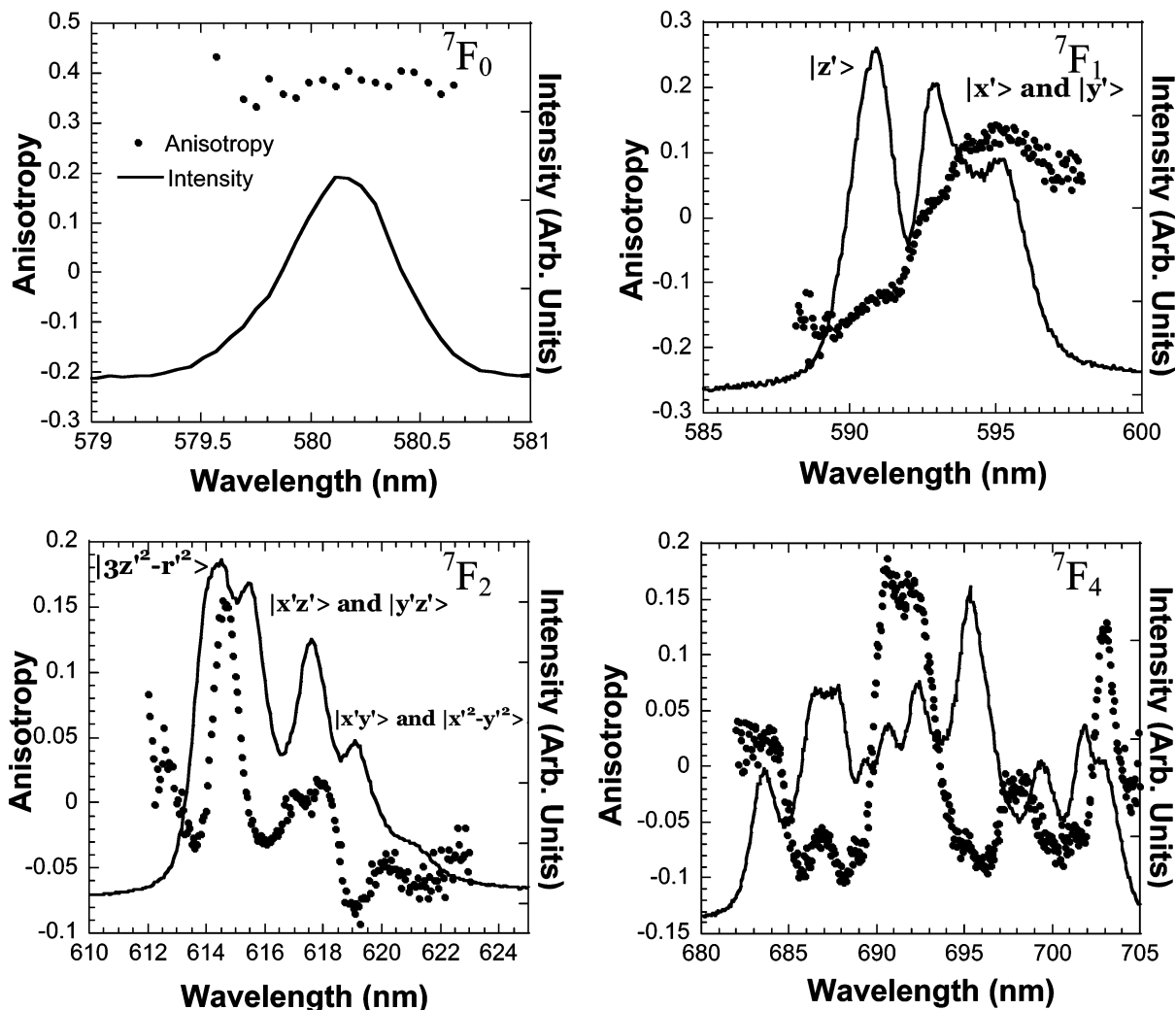
Figure 6. Anisotropy of Eu−TTHA. Anisotropy data are shown as the black dots. The measured intensity (arbitrary units) of each transition is shown with a black line. Each state, ^7F_J, is labeled in the upper right corner of every plot while the wave function is next to the actual spectral line of the transition to the $^7F_1$ and $^7F_2$ states.

not higher order V_{2n}). Furthermore, the V_3 term in the potential, eq 13, contributes to the relevant admixtures of opposite parity that allow the electric dipole transition. For simplicity, let us first consider the anisotropies and splittings that arise solely from V_2, with the opposite parities admixed only by V_1. Once again, degenerate perturbation theory implies that the five $^7F_2$ eigenstates in the presence of V_2 are the Cartesian combinations:

$$|z'x'\rangle \qquad |z'y'\rangle \qquad |x'y'\rangle \qquad (18)$$

and linear superpositions of the two states

$$|3z'^2 - r'^2\rangle \qquad |x'^2 - y'^2\rangle \qquad (19)$$

with mixing proportional to $\alpha - \beta$, the breaking of the rotational symmetry of V_2 about $\hat{z}$.

The shifts of the energies of these states are given in terms of α, β, and γ by

$$\Delta E_{z'x'} = -\frac{2}{7}\beta \quad \Delta E_{z'y'} = -\frac{2}{7}\alpha \quad \Delta E_{x'y'} = -\frac{2}{7}\gamma \quad (20)$$

while the latter two states are shifted by

$$\Delta E = \pm\frac{2}{7}\left(\gamma^2 + \frac{1}{3}(\alpha - \beta)^2\right)^{1/2} \qquad (21)$$

TABLE 2: Theoretical and Experimental Values of the Anisotropy of Eu−DTPA−cs124[a]

wave functions	wavelength[b] (nm)	calculated anisotropy	measured anisotropy	calculated relative intensity
		$^7F_0$ State		
$|Y_{00}\rangle$	581.0	0.06	0.08	1.0
		$^7F_1$ State		
$|x'\rangle$	594.8	0.04	0.04	0.33
$|y'\rangle$	596.0	0.06	0.06	0.33
$|z'\rangle$	590.8	−0.09	−0.09	0.33
		$^7F_2$ State		
$|3z'^2 - r'^2\rangle$	615.4	0.08	0.04	0.62
$|z'y'\rangle$	618.0	−0.16	−0.05	0.16
$|z'x'\rangle$	618.9	0.10	−0.05	0.16
$|x'y'\rangle$	622.1	−0.20	0.09	0.03
$|x'^2 - y'^2\rangle$	620.4	0.11	0.09	0.03

[a] Columns 3 and 4 compare the calculated value vs the measured value of the anisotropy for Eu−DTPA−cs124. The relative intensity was determined from the square of the emission dipole moment: $|\vec{v}|^2$. [b] The $^7F_0$ and $^7F_1$ wavelengths listed are the measured values. The splittings of the $^7F_2$ state are the same as for Eu−DTPA and are the calculated value.

where the positive shift is for the state primarily $|3z'^2 - r'^2\rangle$ and the negative shift is for the state primarily $|x'^2 - y'^2\rangle$.

Note that the shift from V_2 averaged over the five states vanishes. With the values of α, β, and γ determined from the
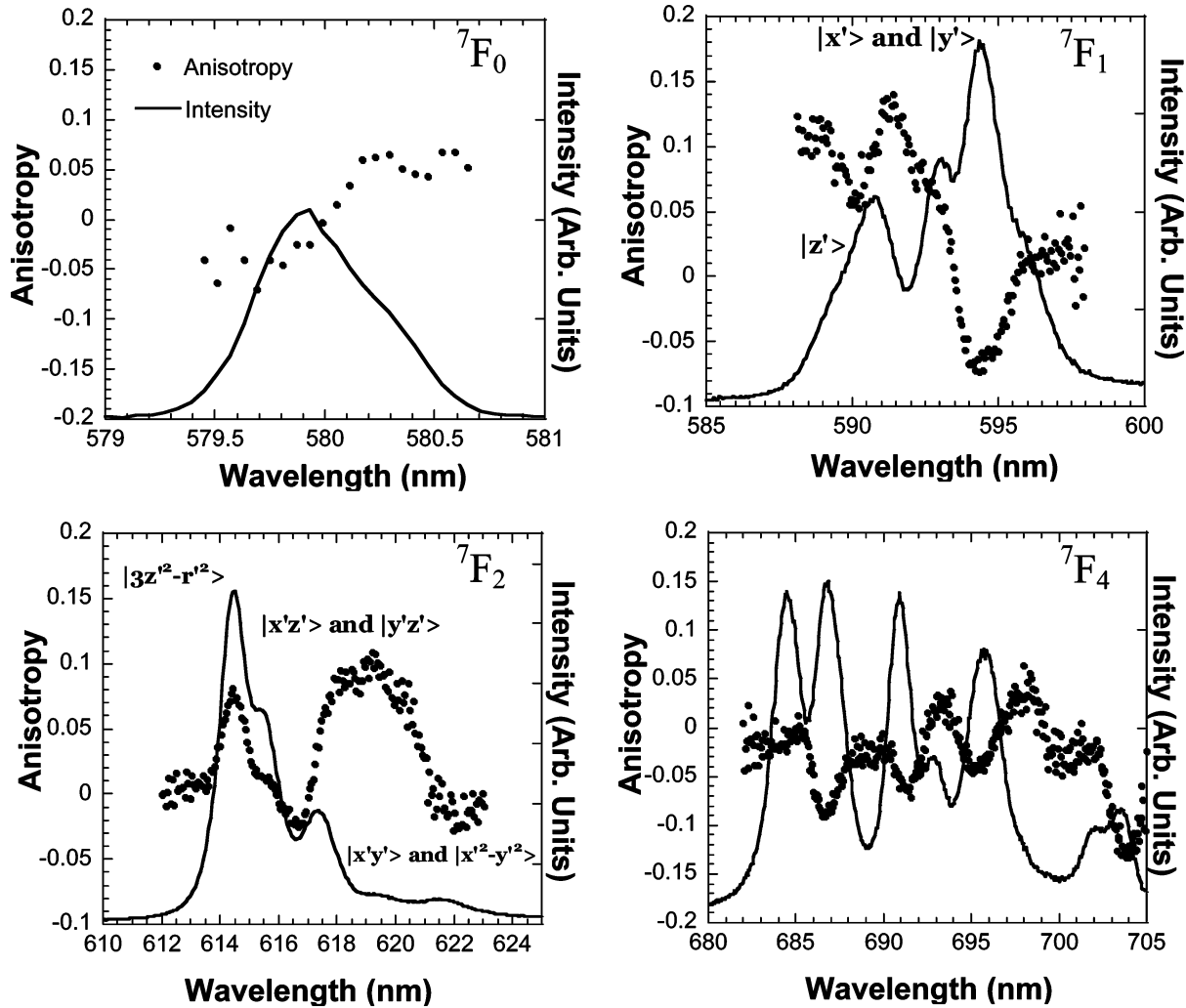
Figure 7. Anisotropy of Eu−TTHA−cs124. Anisotropy data are shown as the black dots. The measured intensity (arbitrary units) of each transition is shown with a black line. Each state, ^7F_J, is labeled in the upper right corner of every plot while the wave function is next to the actual spectral line of the transition to the $^7F_1$ and $^7F_2$ states.

TABLE 3: Theoretical and Experimental Values of the Anisotropy of Eu−TTHA^a

wave functions	wavelength^b (nm)	calculated anisotropy	measured anisotropy	calculated relative intensity
		$^7F_1$ State		
$\|x'\rangle$	592.9	0.02	0.02	0.33
$\|y'\rangle$	595.2	0.12	0.12	0.33
$\|z'\rangle$	590.9	−0.14	−0.14	0.33
		$^7F_2$ State		
$\|3z'^2 - r'^2\rangle$	614.5	−0.06	0.10	0.52
$\|z'y'\rangle$	616.9	0.10	−0.01	0.14
$\|z'x'\rangle$	618.7	0.28	0.01	0.17
$\|x'y'\rangle$	620.2	0.04	−0.08	0.085
$\|x'^2 - y'^2\rangle$	618.3	−0.17	−0.06	0.085

^{a} Columns 3 and 4 compare calculated value vs the measured value of the anisotropy for Eu−TTHA. The relative intensities were determined from the square of the emission dipole moment: $|\vec{v}|^2$. ^{b} The $^7F_1$ wavelengths listed are the measured values and used to fit α, β, and γ of the V_2 potential. The values α, β, and γ are then used to calculate the splittings of the $^7F_2$ state.

relative shifts of the $^7F_1$ states, the calculated wavelengths of the transitions to the five states are ~615.4, ~616.2, ~617.0, ~619.9, and ~620.0 nm, where we have taken the average of the five transitions to be at ~ 617.7 nm. The shifts of these lines reproduce the general trend, three lower lines and two

higher, although the splittings are too small. To get a full understanding of the shifts it is necessary to include V_4.

Let us calculate the anisotropies of the $^7F_2$ states taking into account only V_2. Since the $|^5D_0\rangle \rightarrow |^7F_2\rangle$ transitions are electric dipole, we have $\vec{v}_{x'y'} = \langle x'y'|\vec{d}|^5D_0\rangle$, where $\vec{d}$ is the electric dipole operator; the states here include the parity admixture that allows the electric dipole transition. To illustrate the calculation, we consider the transition to the state $|x'y'\rangle$, for which the angular structure of the matrix element is given by

$$\vec{v}_{x'y'} = \langle x'y'|\vec{d}|^5D_0\rangle \sim \int d\Omega(x'y')z\vec{r} \qquad (22)$$

where the factor z results from the parity admixture. To calculate the result, we transform z into the primed frame, writing $z = \vec{r}\cdot\hat{z} = Ax' + By' + Cz'$, where A, B, and C are the direction cosines of the principal axes of V_2. Then

$$\vec{v}_{x'y'} = \int d\Omega(x'y')(Ax' + By' + Cz')\vec{r} \sim (A, B, 0) \qquad (23)$$

in the primed frame. The unit vector $\hat{v}_{x'y'}$ is thus $(A,B,0)/(A^2 + B^2)^{1/2}$.

The determination of $\hat{v}$ for the other four transitions is similar. The anisotropies of the five $^7F_2$ transitions follow from eq 5 by using the same A^2, B^2, and C^2 determined for the $^7F_1$ transition. The anisotropies of the $^7F_2$ levels do not agree exactly with the data. The best fit to the anisotropies of the $^7F_1$ and the $^7F_2$ level
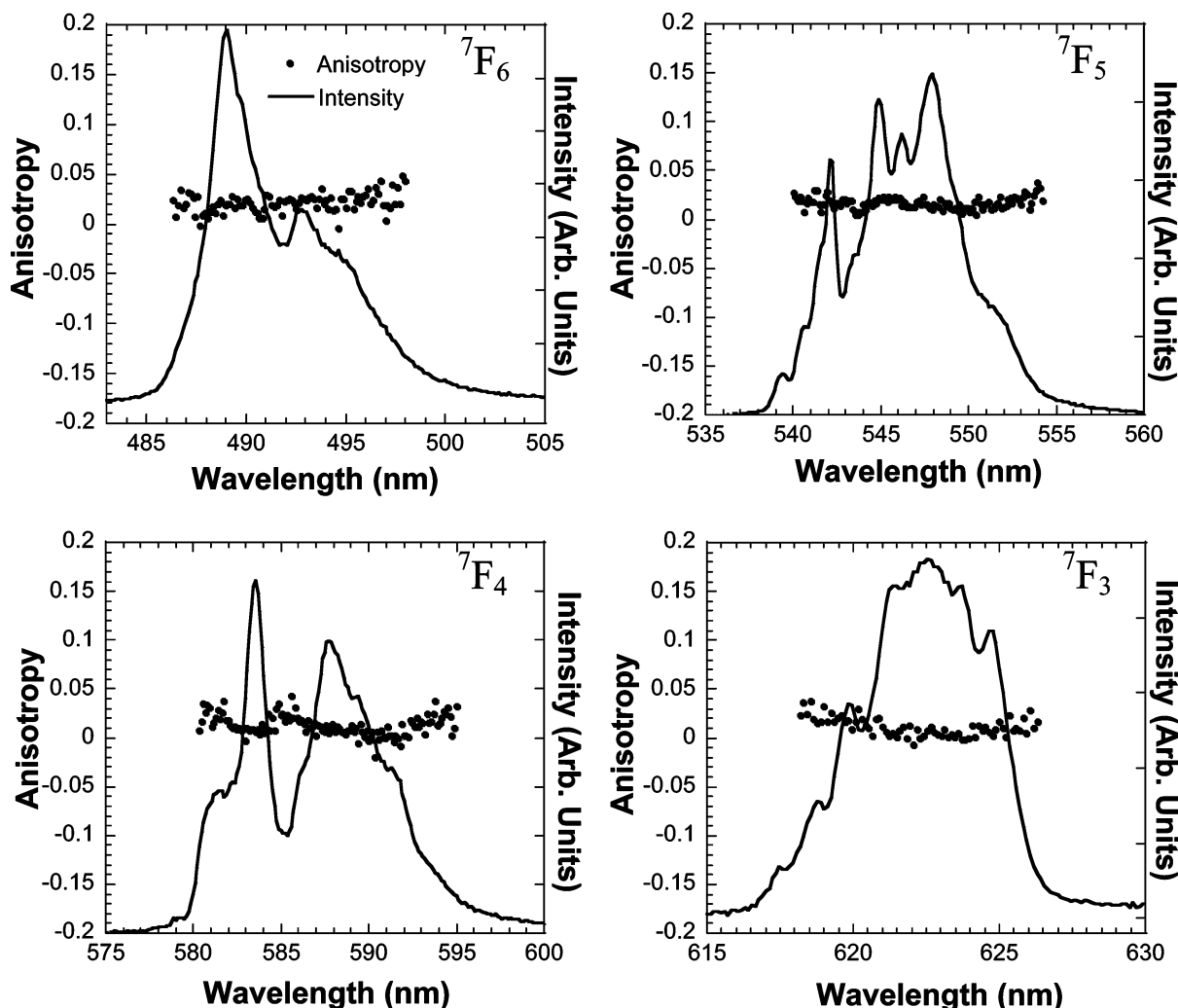
Figure 8. Anisotropy of Tb−DTPA. Anisotropy data are shown as the black dots. The measured intensity (arbitrary units) of each transition is shown with a black line. Each state, ^7F_J, is labeled in the upper right corner of every plot.

TABLE 4: Theoretical and Experimental Values of the Anisotropy of Eu−TTHA−cs124[a]

wave functions	wavelength[b] (nm)	calculated anisotropy	measured anisotropy	calculated relative intensity
		$^7F_0$ State		
$\lvert Y_{00} \rangle$	580.0	−0.11	0.01	1.0
		$^7F_1$ State		
$\lvert x' \rangle$	592.9	0.05	0.05	0.33
$\lvert y' \rangle$	595.2	−0.07	−0.07	0.33
$\lvert z' \rangle$	590.9	0.06	0.06	0.33
		$^7F_2$ State		
$\lvert 3z'^2 - r'^2 \rangle$	614.5	−0.08	0.08	0.52
$\lvert z'y' \rangle$	616.9	−0.11	0.01	0.14
$\lvert z'x' \rangle$	618.7	0.09	0.02	0.17
$\lvert x'y' \rangle$	620.2	0.16	0.1	0.085
$\lvert x'^2 - y'^2 \rangle$	618.3	0.18	−0.01	0.085

[a] Columns 3 and 4 compare the calculated value vs the measured value of the anisotropy for Eu−TTHA−cs124. The relative intensity was determined from the square of the emission dipole moment: $\lvert \vec{v} \rvert^2$. [b] The $^7F_0$ and $^7F_1$ wavelengths listed are the measured values. The splittings of the $^7F_2$ state are the same as for Eu−TTHA and are the calculated value.

is found with the values $A^2 = B^2 \cong 0.08$ and $C^2 \cong 0.84$. The resulting anisotropies for the $^7F_1$ and $^7F_2$ eigenstates are given in Table 1, together with the calculated wavelengths, given in parentheses, of the emitted levels taking only V_2 into account,

and the fractional intensity, which is proportional to $(v_z)^2$ of each transition. Note that only four, rather than five, of the transitions are observed in the $^7F_2$ data. The reason is most likely that the $\lvert z'y' \rangle$ and $\lvert z'x' \rangle$ states are too close together to be separated with our instrument. The calculation at this level predicts that transition from the $^5D_0$ excited state to the $\lvert 3z'^2 - r'^2 \rangle$ eigenstate is the brightest while the transition to the $\lvert x'^2 - y'^2 \rangle$ and $\lvert x'y' \rangle$ eigenstates are the dimmest. However, the relative intensities of the five lines do not agree particularly well with the data. The discrepancies between the theoretical calculations and the experimental data can be fixed through the addition of the V_4 term in the potential. However, taking into account the full nine parameters in V_4 is not productive. Rather, we indicate the general trend by doing a model calculation assuming (without particular justification) a V_4 that would arise if the underlying medium possessed cubic symmetry in the primed frame, i.e.

$$V_4 = \zeta \left(x'^4 + y'^4 + z'^4 - \frac{7}{2} r'^4 \right) \qquad (24)$$

This potential shifts the states $\lvert 3z'^2 - r'^2 \rangle$ and $\lvert x'^2 - y'^2 \rangle$ by an energy, $(^3/_2)e$ (where e is proportional to ς), while the $\lvert z'y' \rangle$, $\lvert z'x' \rangle$, and $\lvert x'y' \rangle$ states are shifted by an energy, $-e$. From the data on the energy splittings of the $^7F_2$ states, we extract an optimal value $e \cong 2.26$ meV, which leads to the wavelengths shown in Table 1 without parentheses. While inclusion of an
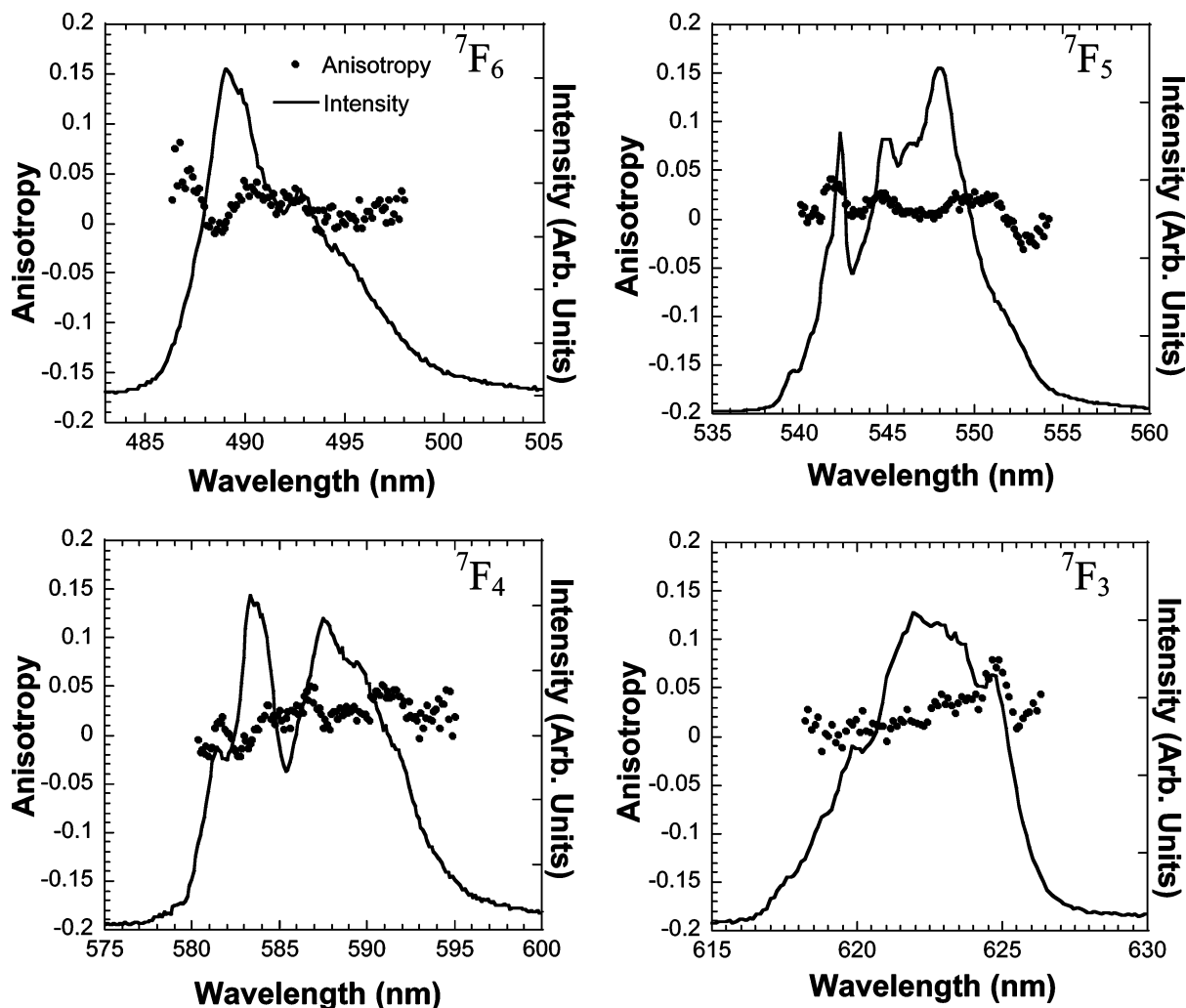
Emission Polarization of Europium and Terbium Chelates

J. Phys. Chem. B, Vol. 107, No. 46, 2003 **12871**

Figure 9. Anisotropy of Tb−DTPA−cs124. Anisotropy data are shown as the black dots. The measured intensity (arbitrary units) of each transition is shown with a black line. Each state, ^7F_J, is labeled in the upper right corner of every plot.

approximate V_4 provides a better understanding of the splitting of the lines within the $^7F_2$ state, we did not calculate its effect on the relative intensities of the transitions or the mixing of the states and hence the anisotropy.

Furthermore, we made no attempt to understand the anisotropy of the $^7F_4$ states. To do so requires including terms V_1, V_3, V_5, and V_7, which are responsible for admixing states to allow the electric dipole transition, and V_2, V_4, V_6, and V_8 to determine the eigenstates and eigenenergies of the $^7F_4$ manifold.

Eu−DTPA−cs124. As Figure 5 shows, the addition of the carbostyril antenna to Eu−DTPA tends to lower the measured anisotropies of the original system toward zero. With the antenna in place, the europium atom is no longer responsible for absorbing the incident excitation photon, now at 337 nm. Instead this process is carried out through excitation of the antenna, which eventually transfers the energy to the europium ion, producing the characteristic Eu^{3+} spectrum. The addition of the antenna changes the absorbing dipole moment of the system. No longer is this dipole moment along the z direction, but is instead in a random direction defined by

$$\hat{u} = P\hat{x}' + Q\hat{y}' + T\hat{z}' \qquad (25)$$

where $P^2 + Q^2 + T^2 = 1$. Unlike in the case of Eu−DTPA, it is more convenient to write the absorbing dipole moment in the (primed) frame of V_2. The anisotropy of the $^5D_0 \rightarrow {}^7F_0$ and $^5D_0 \rightarrow {}^7F_1$ transitions allow us to determine P, Q, and T. Since

the magnetic dipoles responsible for the emission to the $^7F_1$ states are given by $\hat{x}'$ for $|x'\rangle$, $\hat{y}'$ for $|y'\rangle$, and $\hat{z}'$ for $|z'\rangle$, we find from eqs 9 and 11 and the measured anisotropies of the $^7F_1$ states that the direction of u is constrained by $P^2 \cong 0.27$, $Q^2 \cong 0.24$, and $T^2 \cong 0.49$.

To extract the signs of the direction cosines, we note that the anisotropy of the $^5D_0 \rightarrow {}^7F_0$ transition is given by

$$r = \frac{3}{5}(AP + BQ + CT)^2 - \frac{1}{5} \qquad (26)$$

where A, B, and C are the direction cosines determined from Eu−DTPA. The values $P \cong 0.52$, $Q \cong -0.49$, and $T \cong 0.70$ give the best match to the data. The fact that P^2 and Q^2 are slightly different is reflected in the anisotropies of the states $|x'\rangle$ and $|y'\rangle$, which are not quite equal (unlike in the Eu−DTPA complex).

We apply the same procedure to the $^7F_2$ spectrum, using $\hat{u}$ from eq 25, and the results are in Table 2. Since the $|z'y'\rangle$ and $|z'x'\rangle$ states are so close in wavelength and hence not resolved, there is a sharp drop in anisotropy in both Eu−DTPA and Eu−DTPA−cs124. Once again agreement between the measured and calculated anisotropies and the spectrum of the $^7F_2$ states can be improved by including V_4; we did not do this due to the complexities of such a potential. It should be noted that the $|x'y'\rangle$ and $|x'^2 - y'^2\rangle$ states are split a little more in Eu−DTPA than in Eu−DTPA−cs124, a splitting which probably indicates
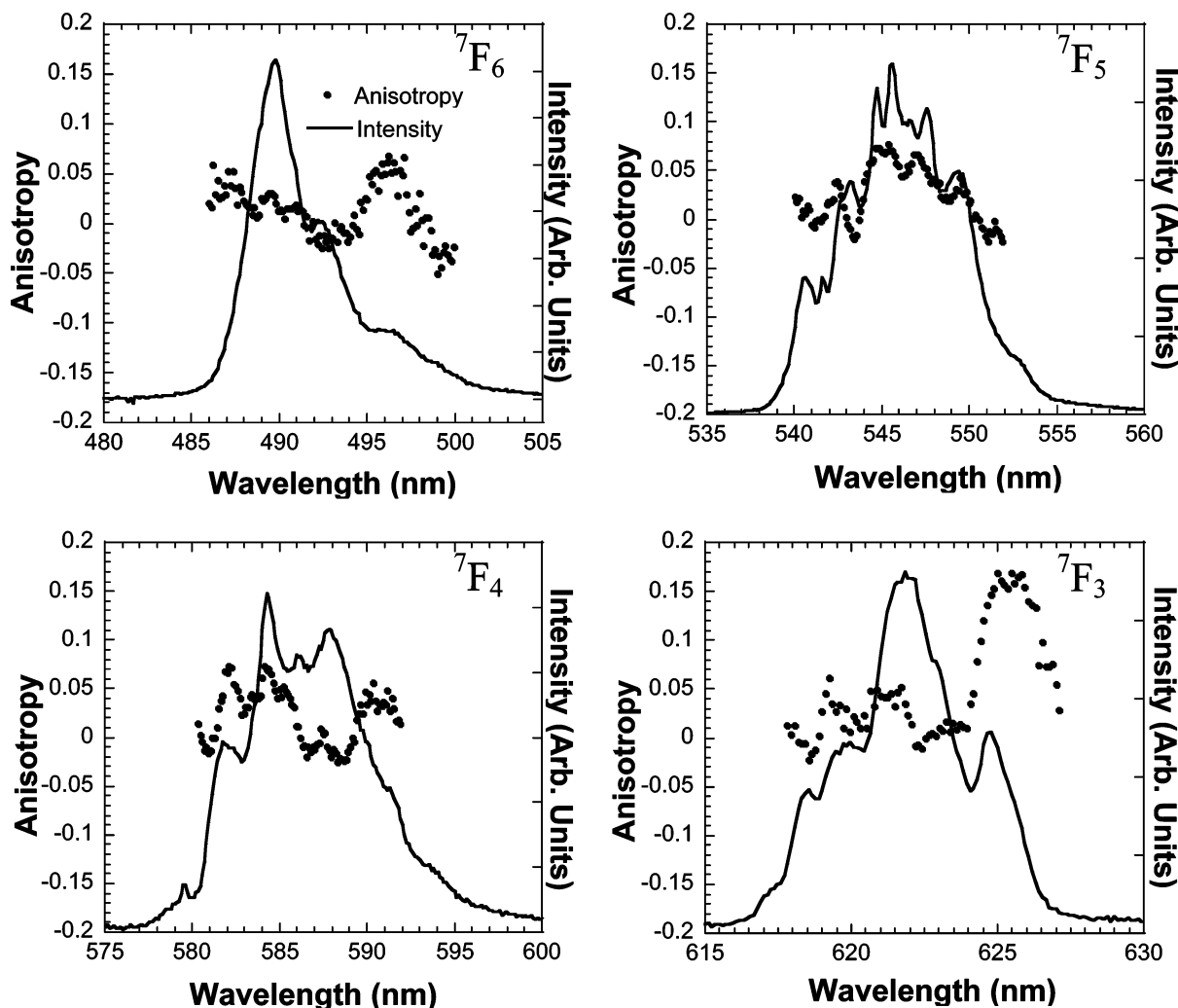
Figure 10. Anisotropy of Tb−TTHA−cs124. Anisotropy data are shown as the black dots. The measured intensity (arbitrary units) of each transition is shown with a black line. Each state, ^7F_J, is labeled in the upper right corner of every plot.

slight differences in V_2 and V_4 between Eu−DTPA and Eu−DTPA−cs124.

Eu−TTHA and Eu−TTHA−cs124. The structure of TTHA, shown in Figure 1, is essentially the same as that of DTPA but with one additional amino-carboxylate group. The same theory for TTHA as for DTPA can be applied to understand the splitting of the states and the corresponding anisotropies. Figure 6 shows that, as in Eu−DPTA, the $^7F_0$ state has an anisotropy of 0.38 ± 0.01, compared with the expected value 0.4, since $\hat{u}$ and $\hat{v}$ are parallel; the anisotropy is probably decreased by a slight rotation of the sample during the millisecond lifetime of the intermediate state.

The $^7F_1$ and $^7F_2$ eigenstates are the same for DTPA and TTHA, with similar, but not identical, local field effects. The splittings of the $^7F_1$ transitions can be calculated in terms of V_2 for Eu−TTHA. Figure 6 shows two important differences from the case of Eu−DTPA. First, the splittings of the $^7F_1$ line are not as great between the states $|z'\rangle$ and the $|x'\rangle$, $|y'\rangle$, and second, the anisotropy of the $|x'\rangle$ and $|y'\rangle$ states is no longer approximately equal, and thus $A^2 \neq B^2$. We find the values, $A^2 \cong 0.30$, $B^2 \cong 0.10$, and $C^2 \cong 0.60$. Table 3 lists the calculated wavelengths, anisotropies, and relative intensities, with the same approximate V_4 (eq 24) as used for Eu−DTPA. Unlike in Eu−DTPA, the calculations predict that the state $|x'^2 - y'^2\rangle$ now has a higher energy than $|z'x'\rangle$. It is difficult to determine from the intensity spectrum and the anisotropy data in Figure 6 in

the $^7F_2$ panel whether the $|x'^2 - y'^2\rangle$ state has a higher energy than the $|z'x'\rangle$ state. The fact that the relative intensity for the $|x'^2 - y'^2\rangle$ state is much lower than the relative intensity for the $|z'x'\rangle$ state suggests that this is not the case though. We expect that the agreement between the theory and experiment would be improved with inclusion of V_3 and a fully parametrized V_4.

The measured anisotropy, especially for the transitions to the eigenstates within the $^7F_0$ and $^7F_1$ manifolds, remains essentially unchanged between the DTPA and TTHA chelates. However, upon addition of the antenna we see how the chelate−antenna relationship can drastically affect the anisotropy (e.g., see the $^7F_1$ panel in Figures 5 and 7). The addition of the antenna to Eu−TTHA (data shown in Figure 7) rotates the absorption dipole moment, $\vec{u}$, to a new orientation. The values of P, Q, and T, in eq 25, can once again be determined from the anisotropy of the $^7F_1$ state and then applied to the $^7F_0$ and $^7F_2$ states. The $^7F_0$ state of Eu−TTHA−cs124 seems to have two values for the anisotropy. As has been shown before,[12,15] TTHA has two different species, which create two different environments for the europium atom and lead to an effective splitting of the $^7F_0$ line. Our instrument does not have the resolution to detect such a splitting, but we do see broadening of the $^7F_0$ line in Eu−TTHA−cs124 as well as two distinct values for the anisotropy when compared with Eu−DTPA−cs124. The theoretical values of the anisotropy are shown for Eu−TTHA−cs124 in Table 4. The fact that there are two different species of TTHA

further complicates the calculations, which were done assuming one species for simplicity. Furthermore, the agreement with the measured values would be improved with inclusion of V_3 and a full V_4.

Tb−DTPA and Tb−DTPA−cs124. Figure 8 shows the anisotropies of Tb−DTPA, which are all close to zero. This effect arises from the fact that the ground state is $^7F_6$ and the excited state is $^5D_4$, unlike in Eu^{3+} where the ground state is $^7F_0$ and the excited state is $^5D_0$. The large number of m, J states in the $^7F_6$ and $^5D_4$ manifolds has the effect of creating a large number of absorption dipole moments. Similarly, the final transition can be through a large number of emission dipole moments as well. The extensive number of such differently oriented dipole moments leads to an anisotropy near zero.

Figure 9 shows the anisotropy of Tb−DTPA−cs124; once again the anisotropies are essentially zero. However, the anisotropy increases slightly with the addition of the antenna, especially at 625 nm. This result at first seems unexpected because the addition of the antenna in Eu−DTPA tends to decrease the anisotropies. However, in the case of europium, the addition of the antenna only changes the orientation of the absorption dipole moment, increasing the angle between the absorption and emission dipole moments and thus decreasing the anisotropy. In the case of terbium, excitation through the antenna reduces the number of absorption dipole moments from all the $^7F_6 \rightarrow {}^5D_4$ mJ transitions to just one absorption moment of the carbostyril antenna. Furthermore, due to the orientation of the antenna with respect to Tb−DTPA, probably only a few of the $^5D_4$ states are excited by the antenna, thus decreasing the number of emission dipole moments and hence increasing in anisotropy. This effect is only slight for Tb−DTPA−cs124, but is more significant in the case of Tb−TTHA−cs124, to which we turn later.

Tb−TTHA and Tb−TTHA−cs124. The data for the anisotropy of Tb−TTHA is not shown but is essentially zero for the four lines ($^7F_6$, $^7F_5$, $^7F_4$, and $^7F_3$). The reason for the low anisotropy of Tb−TTHA is the same as was given for Tb−DTPA, i.e., multiple transition dipole moments at different angles. Similar to Tb−DTPA, addition of the antenna increases the anisotropy of Tb−TTHA−cs124 (Figure 10) due to the antenna's orientation selecting only certain $^5D_4$ states to excite, thereby reducing the number of emission dipole moments and increasing the anisotropy. However, in the case of TTHA, the increase is far more significant, especially at 625 nm.

V. Conclusions

The lanthanide chelates with the carbostyril antenna are an important tool that can be used to determine distances through energy transfer to an acceptor dye (LRET). Until this point, it had been assumed that the anisotropy of the lanthanides (especially Tb^{3+}) when bound to the DTPA−cs124 complex would be near zero due to the large number of transition dipole moments of the states. Our measurements clearly show that the

anisotropy of Tb−DTPA−cs124 (and Tb−TTHA−cs124) is indeed near zero and when coupled with a millisecond lifetime will likely be zero at room temperature when bound to a bimolecule of interest.

As for Eu−DTPA, a theoretical understanding of the splittings and the anisotropies of the ^7F_J states can be explained through an application of perturbation theory and the Wigner−Eckhardt theorem. The theoretical calculations match the experimentally measured values quite well. A better agreement could be obtained through a more rigorous application of further perturbative terms in the potential. It had been hoped that upon the addition of the carbostyril antenna, which is a more usable form, Eu−DTPA−cs124 would have some lines (especially the $^7F_0$) that would still have a high anisotropy. If, for example, the $^7F_0$ line still had a high anisotropy upon the addition of the antenna, it could be used as a probe to study slow (i.e., on the order of a millisecond) rotational motion of biological molecules. However, our results show that the anisotropy of Eu−DTPA−cs124 is significantly reduced upon the addition of the antenna and therefore cannot be used as a rotational probe. However, the theory suggests that the angle between the chelate and the antenna can be changed such that the high anisotropy of Eu−DTPA's $^7F_0$ line is retained upon the addition of the antenna. Such probes would be useful for studying rotational motion on the millisecond time scale.

References and Notes

(1) Selvin, P. R. *Annu. Rev. Biophys. Biomol. Struct.* **2002**, *31*, 275.
(2) Cantor, C. R.; Schimmel, P. R. *Biophysical Chemistry*; W. H. Freeman and Co.: San Francisco, 1980; Vol. 2.
(3) Ofelt, G. S. *J. Chem. Phys.* **1962**, *37*, 511.
(4) Judd, B. R. *Phys. Rev.* **1962**, *127*, 750.
(5) Carnall, W. T.; Fields, P. R.; Rajnak, K. *J. Chem. Phys.* **1968**, *49*, 4412.
(6) Gorller-Walrand, C.; Fluyt, L.; Ceulemans, A. *J. Chem. Phys.* **1991**, *95*, 3099.
(7) Drexhage, K. H. *Sci. Am.* **1970**, *222*, 108.
(8) Bunzli, J.-C. G. Luminescent Probes. In *Lanthanide Probes in Life, Chemical and Earth Sciences, Theory and Practice*; Bunzli, J.-C. G., Choppin, G. R., Eds.; Elsevier: New York, 1989; p 219.
(9) Nakazawa, E.; Shionoya, S. *J. Chem. Phys.* **1967**, *47*, 3211.
(10) Gorller-Walrand, C.; Hendrickx, I.; Fluyt, L.; Bunzli, J.-C. G.; Moret, E. *Chem. Phys. Lett.* **1990**, *170*, 223.
(11) Vereb, G.; Jares-Erijman, E.; Selvin, P. R.; Jovin, T. M. *Biophys. J.* **1998**, *75*, 2210.
(12) Li, M.; Selvin, P. R. *J. Am. Chem. Soc.* **1995**, *117*, 8132.
(13) Xiao, M.; Selvin, P. R. *Rev. Sci. Instrum.* **1999**, *70*, 3877.
(14) Lakowicz, J. R. *Principles of Fluorescence*, 2nd ed.; Kluwer Academic: New York, 1999.
(15) Holz, R. C.; Horrocks, W. D. J. *Inorg. Chim. Acta* **1990**, *171*, 193.